Supporting information for: The Controlled-Potential Simulation of Elementary Electrochemical Reactions: Proton Discharge on Metal Surfaces

Georg Kastlunger, Per Lindgren, and Andrew A. Peterson*

School of Engineering, Brown University, Providence, RI, United States

E-mail: andrew_peterson@brown.edu

Computational details

The results in the main article have been computed using the GPAW code,[S1,S2] where both the potential and the wave functions are represented on a real space grid. The grid spacing applied was 0.18 Å and the k-space dispersion was sampled on a 4x6x1 mesh, unless stated otherwise. A Fermi temperature of 0.1 K was chosen and the Perdew-Burke-Ernzerhof (PBE) exchange-correlation functional has been applied.

The metallic surfaces were modeled as 3x2x3 atom slabs, with six atoms in the interface plane. Three layers, with the lowest lying layer fixed at the equilibrium lattice constant, were included in the perpendicular direction. For fcc Au, this bulk lattice constant was determined as 4.18 Å on an 21x21x21 k-point mesh, which is 2.5% larger than the experimental value of 4.08 Å.[S3] Fcc Pt exhibited an equilibrium lattice constant of 3.97 Å. Starting from these surface structures with maximal symmetry, all structures were relaxed until a force convergence criterion of 0.05 eV/Å was reached. In all calculations, a dipole correction has been applied in order to decouple the potential perpendicular to the electrode surface and provide a field-free region for the determination of reference potentials.

The explicit water bilayers under study consist of hexagonal ice-like water geometry.[S4] The hydrogen atom of every second water molecule is pointing either towards (H-down) or

away (H-up) from the metal surface. This geometry has been determined to be the most reasonable representation for DFT studies where thermal averaging is not included.[S4,S5]

As in the main article, the counter charge starts 3 Å above the explicit atoms, and its thickness has been set to ≈8 Å. The parameters defining the implicit solvent were chosen in accordance with the optimized values of Held and Walter, namely u_0=0.180 eV, γ= 18.4 dyn cm^{-1}, T=298 K, ϵ_∞=78.36. The applied van der Waals radii are based on the determined values of Bondi.[S6]

For the creation of the dotted black lines representing the water layer frontier orbitals, DFT calculations of the slab+water system with an LCAO/dzp basis[S7] have been performed. All other parameters have been chosen in the exact same way as described above. In order to retrieve the spacial shape of the MOs the water subspace in the LCAO Hamiltonian was diagonalized and the resulting eigenfunctions representing the HOMO and LUMO, where mapped onto the applied grid. Finally, the square of the two orbitals have been plotted in order to show their contribution to the electron density.

Consistency of SJM with the computational hydrogen electrode model

In the CHE model one calculates the Free or Potential energy change ΔG_0 of a reaction on the basis of the equilibrium

$$\mu(H^+) + \mu(e^-) = \frac{1}{2}\mu(H_2^{(g)}) \tag{1}$$

at $U_{SHE} = 0\ V_{SHE}$. Therefore, ΔG_0 of a reaction involving the recombination of a proton and an electron, i.e. $X^* + H^+ + e^- -> XH^*$ happening at 0 V_{SHE} can be calculated as

$$\Delta G_0^{U_{\mathrm{SHE}}} = G_{XH} - G_{X*} - 0.5 * G_{H_2}^{(g)}. \tag{2}$$

At potentials other than U_{SHE} ΔG_0 can then be retrieved by accounting for the change in driving force and the changed equilibrium in eq. 1. As a consequence ΔG_0 is shifted by eU for a reaction involving one electron, since $0.5 * G_{H_2}^{(g)}$ in eq. 2 changes to $0.5 * G_{H_2}^{(g)} + eU$ in order justify its usage as a substitute for $G_(H^+) + \mu(e^-)$. This leads to

$$\Delta G_0^U = \Delta G_0^{U_{\mathrm{SHE}}} + N_e e U, \tag{3}$$

with N_e, being the number of electrons transferred and e being the (positive) elementary charge.

In the SJM methodology we calculate the reaction enthalpy as

$$\Delta G_0^U = G_{\mathrm{FS}}^U - G_{\mathrm{IS}}^U + \Delta N_e e \Phi_e, \tag{4}$$

where G_{FS}^U and G_{IS}^U correspond to the DFT total energies including the solvation Free energy for the final and initial state, respectively, Φ_e is the electrochemical potential which we set in our simulation and $\Delta N_e = N_{e,\mathrm{FS}} - N_{e,\mathrm{IS}}$. Since the transferred hydrogen is included in both IS and FS we do not have to add $0.5 * G_{H_2}$, in order to be mass (or atom) consistent

in the course of the reaction. However, we explicitly change the number of electrons in the unit cell in the course of the reaction.

Equation 4 can be reformulated in order to make its relation to the CHE model more apparent:

$$\Delta G_0^U = G_{\mathrm{FS}}^U - G_{\mathrm{IS}}^U + \Delta N_e e \Phi_e \tag{5}$$

$$= G_{\mathrm{FS}}^U - G_{\mathrm{IS}}^U + \Delta N_e e U_{\mathrm{SHE}} + \Delta N_e e U \tag{6}$$

From the results shown in the main article it can be retrieved, that the change of ΔG_0^U with potential nearly corresponds to $\Delta N_e e U$, as it would also be predicted by the CHE model. Hence, $G_{\mathrm{FS}}^U - G_{\mathrm{IS}}^U + N_e e U_{\mathrm{SHE}}$ has to be potential independent. That is the case for $\Delta N_e e U_{\mathrm{SHE}}$, if ΔN_e stays constant over the investigated potential range, which has been shown to be the case in Figure 10 of the main article. However, the potential (in)dependence of $G_{\mathrm{FS}}^U - G_{\mathrm{IS}}^U$ is not so apparent, since in SJM both G_{FS}^U and G_{IS}^U exhibit a substantial individual potential dependence. In order for the subtraction to be independent of U the following condition has to be valid:

$$\frac{\partial G_{\mathrm{FS}}^U}{\partial U} \stackrel{!}{=} \frac{\partial G_{\mathrm{IS}}^U}{\partial U}. \tag{7}$$

Equation 7 can now be rewritten into

$$\left(\frac{\partial G_{\mathrm{FS}}^U}{\partial N_e}\right)\left(\frac{\partial N_e}{\partial U}\right)_{\mathrm{FS}} \stackrel{!}{=} \left(\frac{\partial G_{\mathrm{IS}}^U}{\partial N_e}\right)\left(\frac{\partial N_e}{\partial U}\right)_{\mathrm{IS}}, \tag{8}$$

with N_e being the number of electrons or charge.

$\left(\frac{\partial G}{\partial N_e}\right)$ by definition corresponds to the chemical potential μ. In our methodology corresponds to $-\Phi_e$, which being an input in the simulation is the same for both IS and FS. This leaves the condition

$$\left(\frac{\partial N_e}{\partial U}\right)_{\mathrm{FS}} \stackrel{!}{=} \left(\frac{\partial N_e}{\partial U}\right)_{\mathrm{IS}}, \tag{9}$$

which again corresponds to the need of the slopes of the linear functions in Figure 10 of the main article to be the same. We found that this is essentially the case. Therefore, it can be concluded that SJM is consistent with the thermodynamical foundation of the CHE model.

Workflow in the SJM model

The standard workflow in SJM is shown in Figure S1 based on the example of a structure optimization. However, it could be used for any kind of operation which is based on a converged SCF cycle. The crucial part for performing a constant potential simulation is the highlighted loop, which we called the computational potentiostat. In detail the workflow consists of the following steps:

1. Define the parameters of the calculation in the input. These parameters include the

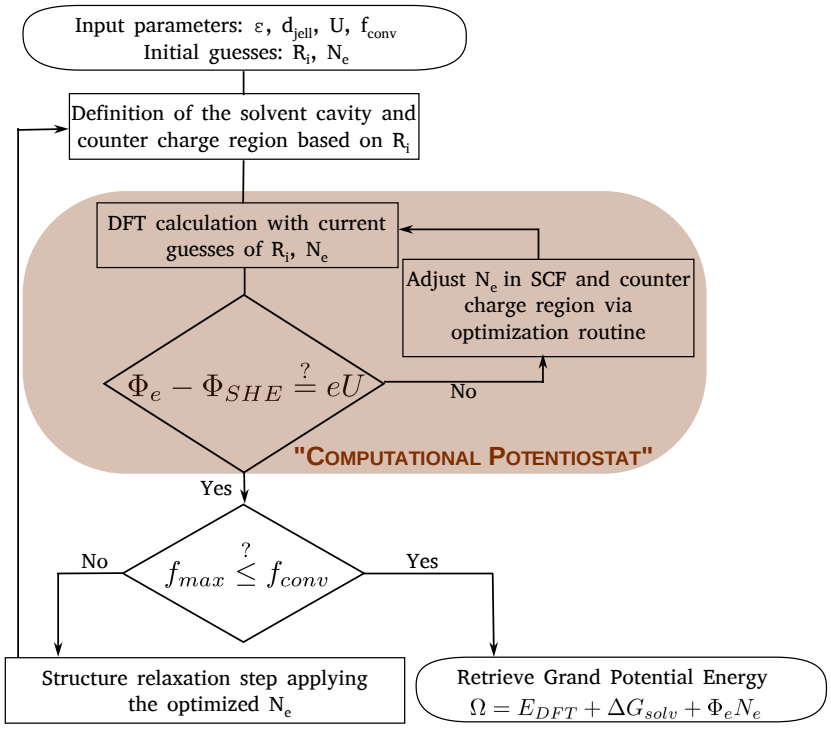

Figure S1: Workflow diagram in the SJM method for the example of a structure optimization

standard SCF parameters such as basis set, **k**-mesh and XC functional and parameters as part of SJM, being the dielectric constant of the applied solvent (ϵ), the desired thickness of the counter charge region (d_{jell}) and the desired electrode potential (U). Additionally, the initial geometry of the atomic system under study and an initial guess for the charge added to the SCF cycle (N_{e}) and the counter charge region, which are equal in magnitude but opposite in sign, is chosen.

2. The SJM algorithm defines the solvent cavity based on the implicit solvent model applied.[S8] Additionally, it also defines the lower boundary of the counter charge based on the atomic positions, if not given explicitly.

3. A first DFT calculation is performed based on the input given in (1), and the electrode potential related to the initial guess of N_{e} is retrieved.

4. The resulting potential (Φ_{e}) is compared to the desired potential and if it does not match, then N_{e} is slightly changed. A second DFT calculation is performed with the new number of electrons, applying the converged wave functions of (3) as a starting guess.

5. The slope of electrode potential versus charge is estimated by $(\Phi_{\text{e}}^{(2)} - \Phi_{\text{e}}^{(1)})/(N_{\text{e}}^{(2)} - N_{\text{e}}^{(1)})$, where the superscripts refer to the 1st and 2nd calculations above.

6. A third DFT calculation is performed with the number of electrons corresponding to the desired potential, as calculated from the slope of (5).

7. If the desired potential has been reached the forces on the atoms are accepted and fed to the atomistic routine, such as BFGS, to propose the next ionic step.

8. The next DFT calculation is performed with the same N_e as the previous. If the potential changed due to the change in geometry, a new N_e is proposed based on the previously stored value of the slope, and the slope is updated accordingly based upon the new value of Φ_e. This is repeated indefinitely until the atomistic algorithm (such as structure optimization) has converged.

An automatized algorithm in the framework of ASE/GPAW can currently be downloaded from git@bitbucket.org:gkastlun/solvated-jellium-method.git and will be implemented into GPAW in the near future.

Computational expense

From the workflow described above, one might conclude that a threefold increase in computational effort is created by the algorithm. This would be the case if, at each ionic step, N_e were guessed randomly for the first DFT calculation, perturbed randomly in a second DFT calculation to get a slope, and then set to its correct value in a third independent DFT calculation.

However, in practice, three effects make the computational effort much less. First, since the atomic structure typically changes only subtly between ionic steps in most atomistic routines (like geometry optimization), the value of N_e to reach a particular potential changes very little, and frequently several ionic steps can be taken at a single N_e before the potential drifts out of the user-specified tolerance. Second, the slope changes little between images (as shown in the bottom panel of Figure S2 and regarding that the correction is typically less than $0.1e^-$). Therefore, when the potential does drift out of tolerance, we can re-use the previous slope estimate to provide the new guess of N_e; this typically brings the potential back to within tolerance with a single additional DFT calculation. Simultaneously, these two points on the same image give a new slope which can be used the next time a slope estimate is used. Third, the wavefunctions of a previous calculation can always be used as a starting point for the SCF cycle. When the same structure is re-run with only a subtly changed value of N_e, these wavefunctions are an excellent initial guess and the DFT calculation converges in relatively few SCF steps.

Figure S2 shows an example of a structure optimization of the Au(111) slab + H-down water interface. In total, 24 ionic steps were needed with the Broyden-Fletcher-Goldfarb-Shanno (BFGS) optimization algorithm to reach a force convergence criterion of 0.05 eV/Å. The total number of SCF cycles added up to 43 in the example, which corresponds to a factor of 1.79, compared to the number of force calls. However, due to the initial starting guess in the SCF cycles, being the converged wavefunctions of the previous step, the number of iterations in potential equilibration steps are reduced, drastically, as can be seen in the right panel of Figure S2. The two characteristics combined lead to a total computational time increase that generally falls below a factor of 1.5.

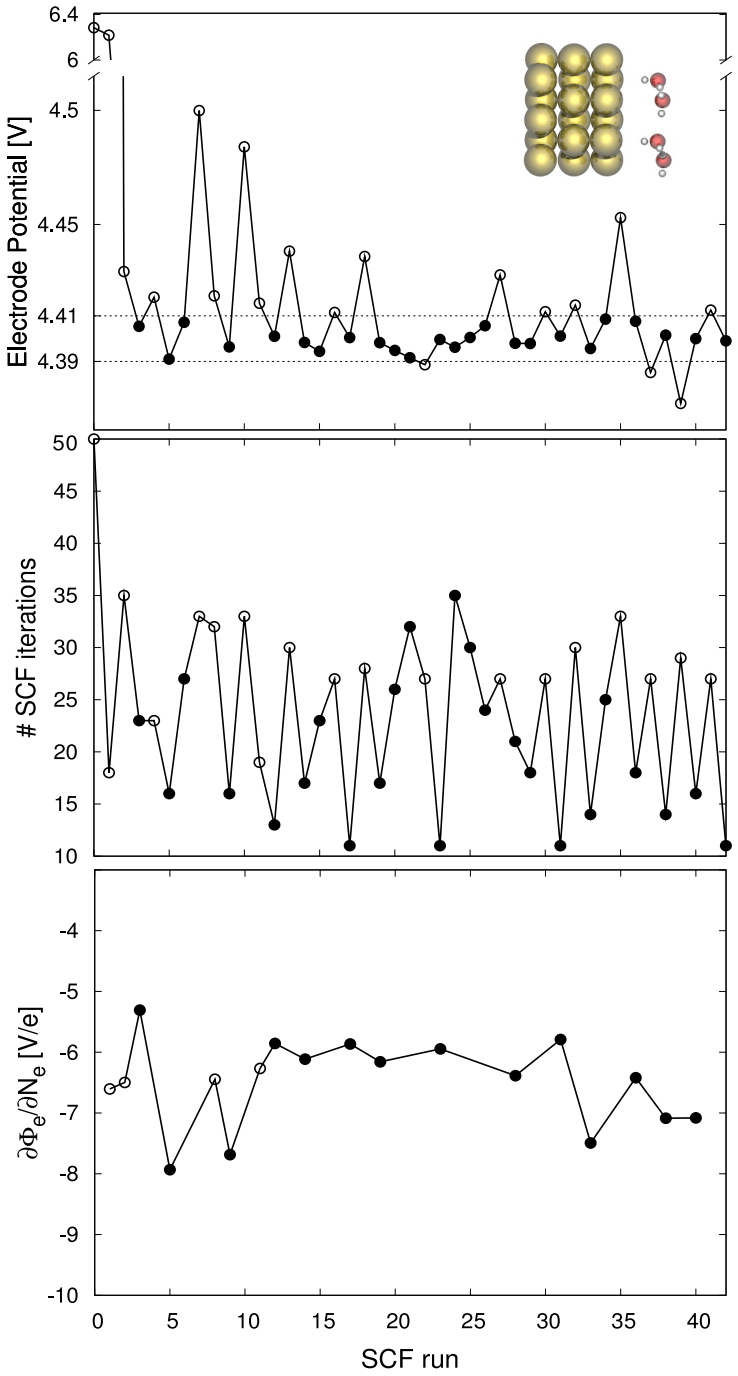

Figure S2: Electrode Potential (top) and number of needed SCF iterations (middle) per SCF cycle, as well as the calculated derivatives of the electrode potential with respect to the number of electrons (bottom) in the course of a structure optimization of the Au(111) slab + H-down water interface. Closed circles represent SCF runs which resulted in the desired potential and a force call was performed, open circles stand for SCF runs which resulted at a potential outside of the tolerance of 10 mV and therefore, lead to a change in N_e instead of positions.

Minimum energy pathways as functions of potential

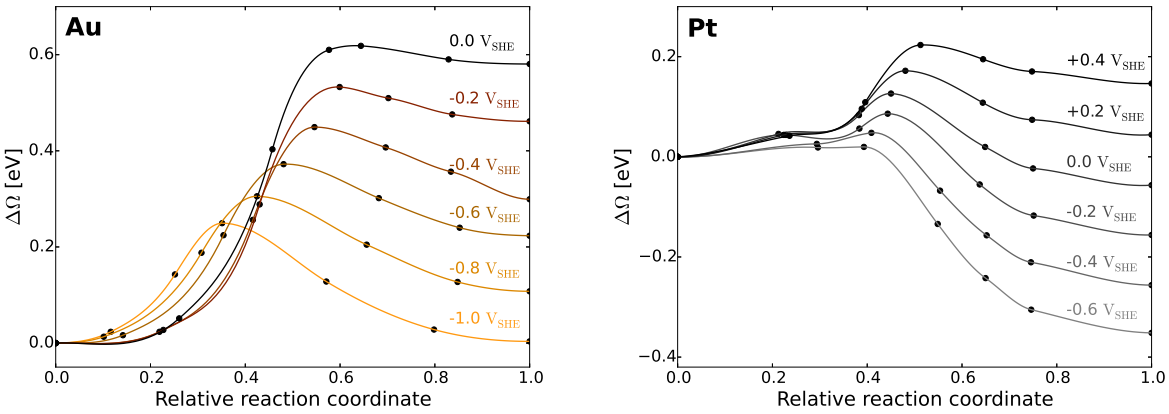

Figure S3: Potential-dependent minimum energy pathways of the Volmer step of HER on Au(111) and Pt(111).

The minimum energy pathways in Figure S3 were calculated using the climbing-image nudged elastic band (CI-NEB) method. The reaction energy and barrier height are higher on Au(111) for each applied potential, and the transition state appears later than on Pt(111). Both metals exhibit the same trend; the transition state moves towards the initial state and the barrier height decreases when the overpotential increases. These trends are indicative of a change in the Butler-Volmer symmetry factor.

Work functions at different applied charges

Figures S4 and S5 show the electrostatic potentials relative to the Fermi level of charged systems for Au(111) and Pt(111), respectively. For both metals, addition/subtraction of electrons to/from the system results in a dramatic change in the work function of the front side of the electrode. The respective values correspond to the points shown in Figures 3 and 6. The back side of the electrode, on the other hand, is unaffected by the charging, leading to the work function being constant at 5.2 and 5.7 eV for Au(111) and Pt(111), respectively.

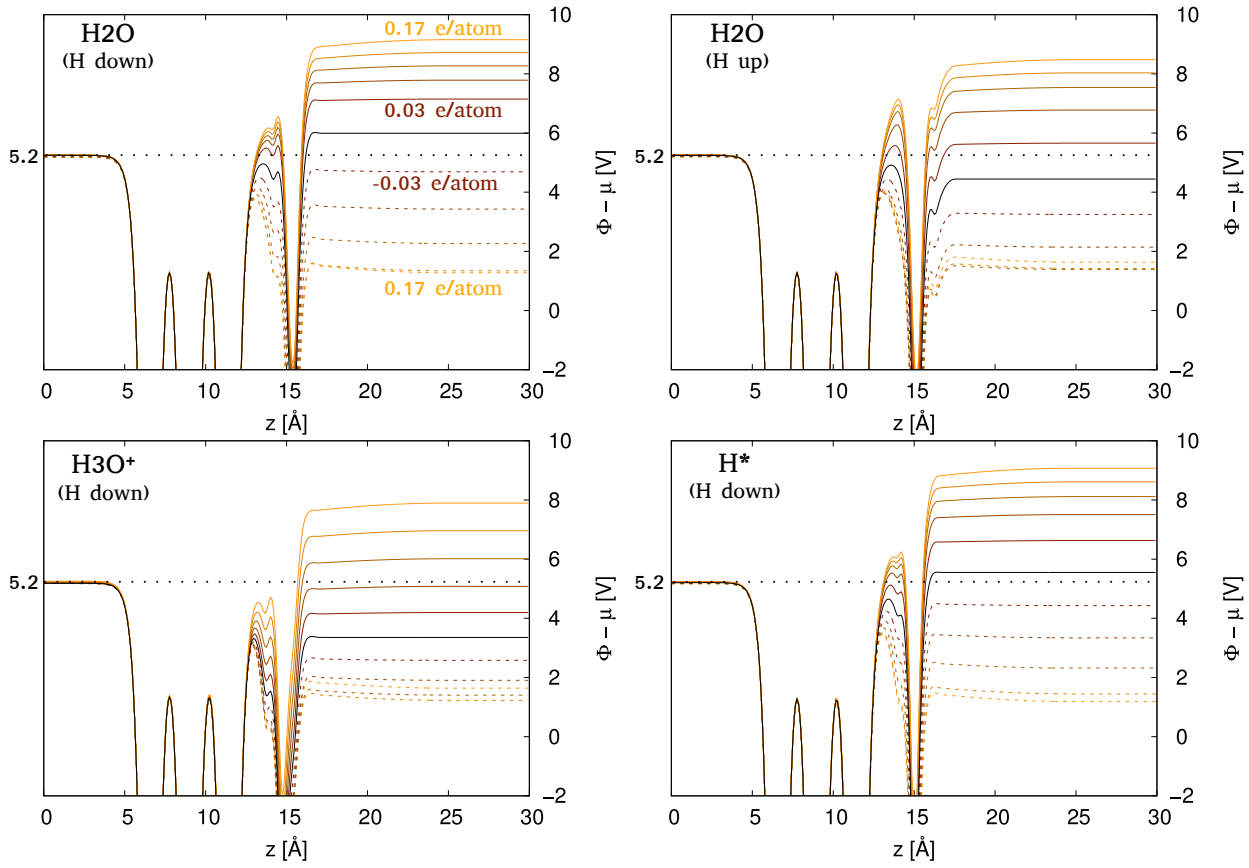

Figure S4: Electrostatic potentials for the H-down and H-up geometries as well as the initial and final states of the Volmer step on Au(111). The electrostatic potential is plotted relative to the Fermi level of the system. The work function on the back side of the electrode is unaffected by the charging.

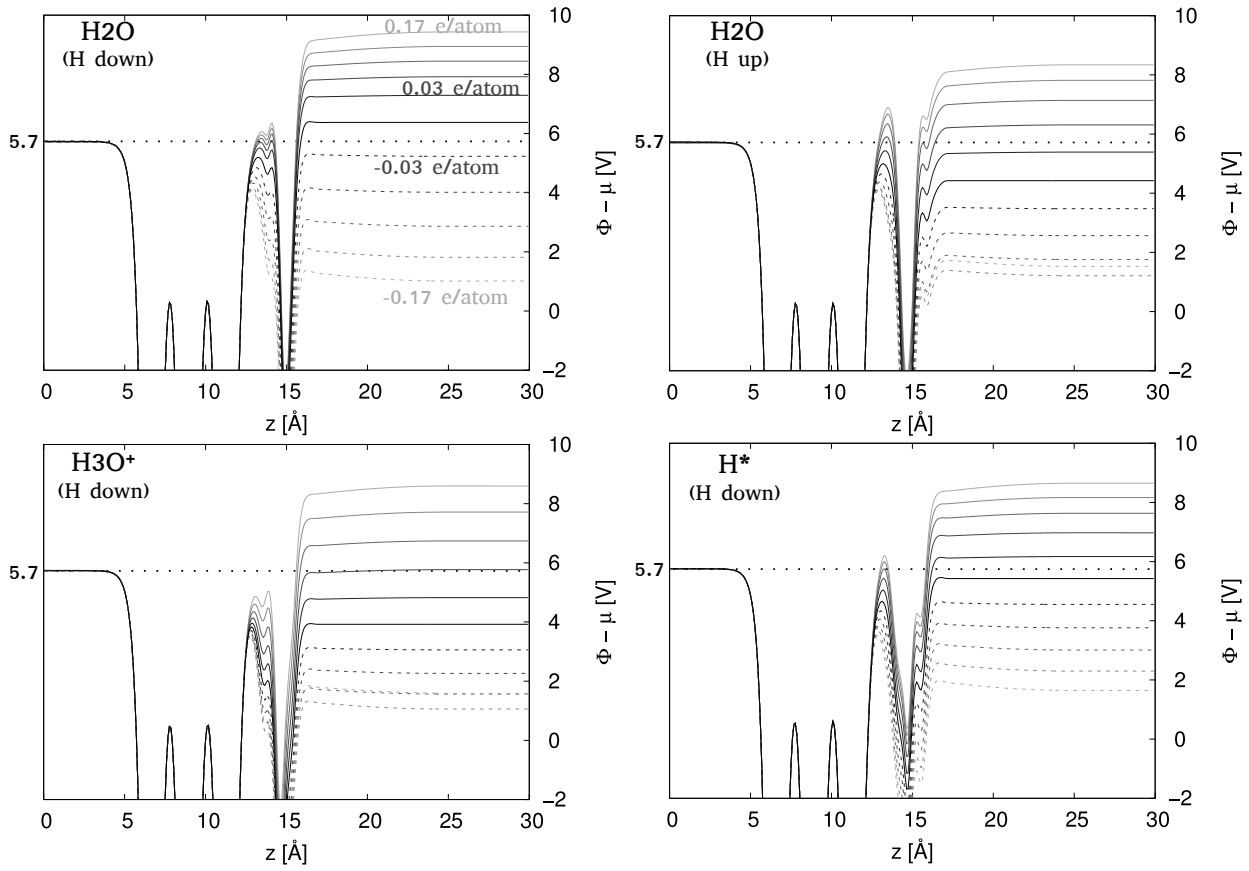

Figure S5: Electrostatic potentials for the H-down and H-up geometries as well as the initial and final states of the Volmer step on Pt(111). The electrostatic potential is plotted relative to the Fermi level of the system. The work function on the back side of the electrode is unaffected by the charging.

Analysis of charge localization based on density of states

In order to explain the finding that only the water interface region of the metallic slabs is charged on a more fundamental level, we have also studied the densities of states projected onto the metal bands composing the two surfaces of the slab. As mentioned in the main article, electron density differences, Bader charge analysis and the work functions of the charged systems indicate that the applied charge always localizes at the interface region, while the back side of the metal slab does not change its surface charge. Unfortunately, projected densities of states (PDOSes) derived from converged grid basis calculations, mapped on the basis of the projector overlaps in the PAW approach, which are no orthonormal basis, can not be applied quantitatively for retrieving the number of electrons via integration up to the system's Fermi level. They can, however, still be applied for the analysis of trends and relative changes in local occupation.

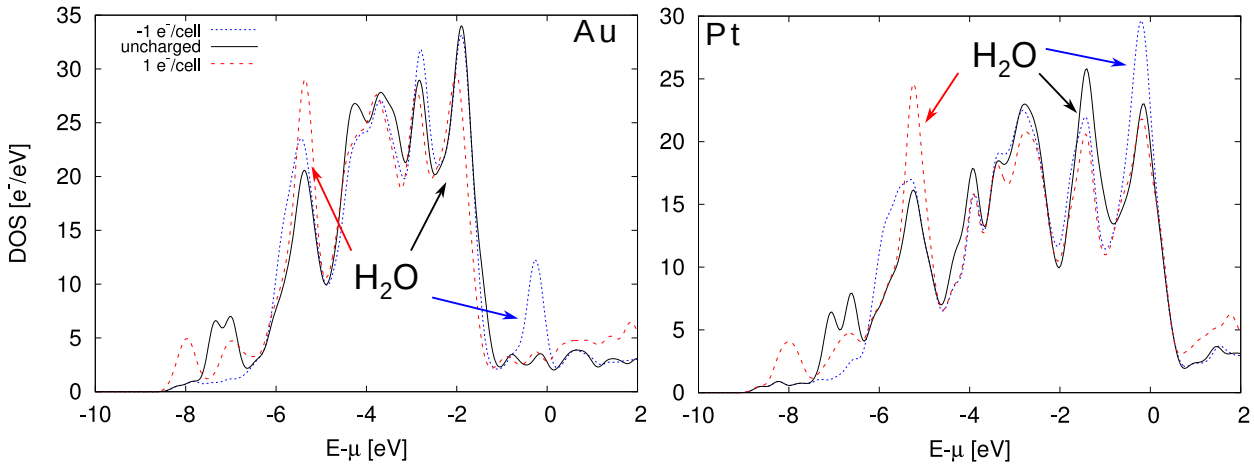

Figure S6: Densities of states of the slab + H_2O down structure for the Au and Pt systems. The situations 0 (black solid), 1 (red dashed) and -1 (blue dotted) added electron to the unit cell are shown. Peaks related to the water HOMO, which appear in the total DOS, have been marked with colored arrows indicating the respective charge state.

Figure S6 shows the densities of states (DOS) of the two metallic slabs. As an example the slab-H_2O down interface structures on Au and Pt have been chosen. Since the applied charges are very low in magnitude compared to the number of valence electrons in the systems, we also provided the number of electrons on the backside and interface region (front) of the electrodes as calculated from an integration over the respective PDOSes in Table S1. In both metal systems the back side of the electrode facing the vacuum does not change the number of electrons in a specific pattern, but does rather exhibit a certain degree of noise. The front side (slab/water interface) on the other hand varies its occupation following the trend created by the applied charge. The noise seems to be mostly canceled in the difference between front and back side and, although the absolute numbers shown in Table S1 should not be given a high weight, the trends are in line with the findings in the electrostatic potentials, Bader charge analysis and electron density differences indicating the described asymmetry in charging.

Table S1: Integrals over the projected densities of states related to the states of the electrode atoms on the two respective surfaces. All the values are given in electrons per unit cell, with the sole exception of the electrode potential given in V. Δ = Front - Back shows the asymmetry in charging. The charge selective regions are located between the horizontal dashed lines.

Excess	Au				Pt			
electrons	Potential	Back	Front	Δ	Potential	Back	Front	Δ
-1.0	9.15	76.10	75.66	-0.43	9.43	114.81	114.47	-0.34
-0.5	8.03	76.15	75.82	-0.33	8.19	114.76	114.53	-0.23
-0.4	7.78	76.26	75.96	-0.30	7.92	115.04	114.83	-0.20
-0.3	7.50	76.23	75.96	-0.27	7.62	115.16	114.99	-0.17
-0.2	7.15	76.29	76.08	-0.21	7.29	115.04	114.91	-0.13
-0.1	6.62	76.26	76.14	-0.12	6.89	114.74	114.68	-0.07
0	5.99	76.11	76.11	0.0	6.37	115.22	115.24	0.02
0.1	5.34	76.23	76.36	0.12	5.80	115.09	115.21	0.12
0.2	4.68	76.23	76.47	0.24	5.21	115.22	115.44	0.22
0.3	4.05	76.21	76.57	0.35	4.61	114.98	115.31	0.32
0.4	3.43	76.17	76.63	0.46	4.01	114.91	115.34	0.43
0.5	2.83	76.09	76.64	0.55	3.43	114.77	115.30	0.53
1.0	1.28	76.06	76.82	0.76	1.01	115.16	116.00	0.84

Charge localization without explicit water

In the absence of explicit water, the charging occurs exclusively at the front side of the electrode. The states on the back side of the electrode are affected by the charging, and the work function is thus constant. Figure S7 shows the electron density and excess electrons of charged systems relative to an uncharged system without explicit water. It is evident that any change to the electron density occurs at the front side of the electrode. Subsequently, all changes in occupation occur at the front side of the electrode.

The implicit solvent model

In the implicit solvent approach of Held and Walter[S8] approach, $\epsilon(\mathbf{r})$ is defined by an effective potential, which is based on the repulsive branch of the Lennard-Jones potential, namely

$$u_{\text{eff}}(\mathbf{r}) = u_0 \sum_a \left(\frac{R_a^{\text{vdW}}}{|\mathbf{r} - \mathbf{R}_a|} \right)^{12}, \tag{10}$$

where $\mathrm{R}_a^{\text{vdW}}$ and $\mathbf{R}_a$ are the van der Waals radii and positions of the atomic species in the unit cell, and u_0 is a scaling parameter introduced in order to fit the molecular cavity size to experimental values for the partial molar volumes of the solute. The relation between $\epsilon(\mathbf{r})$ and u_{eff} is defined by a distribution function

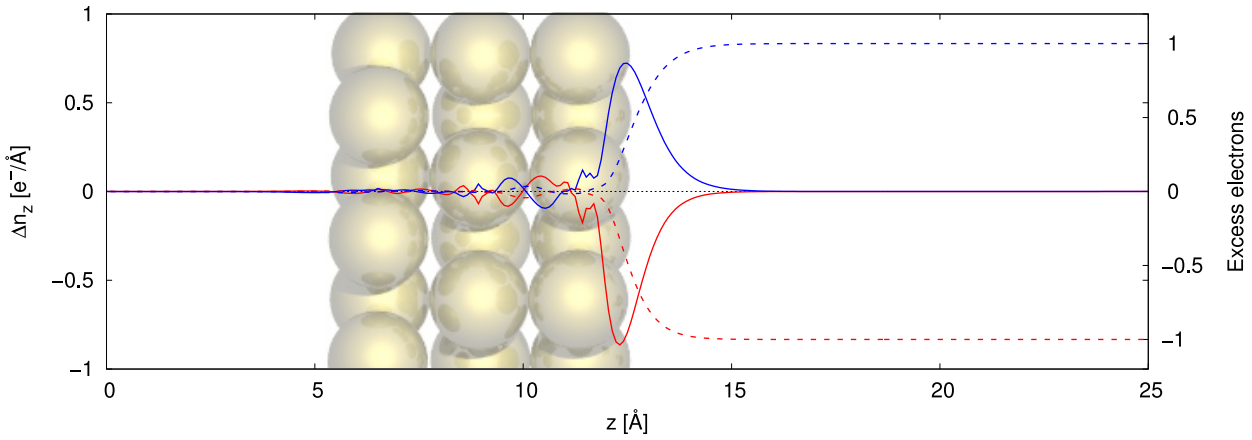

Figure S7: Electron density (—) and excess electrons (- -) of charged systems relative to an uncharged system of the same geometry without explicit water.

$$g_{\text{eff}}(\mathbf{r}) = \exp\left(-\frac{u_{\text{eff}}(\mathbf{r})}{k_{\text{B}}T}\right) \tag{11}$$

and finally

$$\epsilon(\mathbf{r}) = 1 + (\epsilon_\infty - 1)\, g_{\text{eff}}(\mathbf{r}), \tag{12}$$

where ϵ_∞ corresponds to the macroscopic dielectric constant of the solvent.

In SJM we additionally add a contribution to u_{eff} of the form

$$u_{\text{eff}}(\mathbf{r})_{r_z < z_{Au}} = \infty. \tag{13}$$

This constraint ensures that the back side of the electrode is solvent free.

Figure S8 shows an example of the solvation cavity for a Au slab electrode with an explicit water overlayer, where the solvent is present (indicated by $\epsilon > 1$) only on the reactive side of the electrode and increases smoothly to a value of 78.36, chosen as that of room-temperature water. The slight bump around 15 Å is a consequence of the averaging over the xy-plane, where the implicit solvent penetrates slightly into the center of the hexagon created by the water bilayer.

Double layer capacity studies

Figure S9 shows the results gotten from the study on the double layer capacitance of Au(111) and Pt(111) applying SJM. The slope of the curves corresponding to the double layer capacitance, has shown to be slighlty deviating from a constant, due to the nonlinearity in the curves. This behavior is not surprising and has already been described by Sundararaman et al.[S9] Additionally values experimentally determined in EIS studies often show a functional

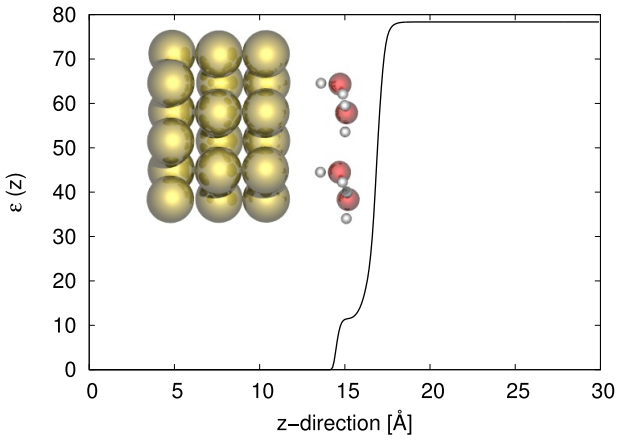

Figure S8: Smooth permittivity function $\epsilon(z)$ for the electrode and adsorbed H_2O in the down bilayer structure, where average values for the xy-plane are shown.

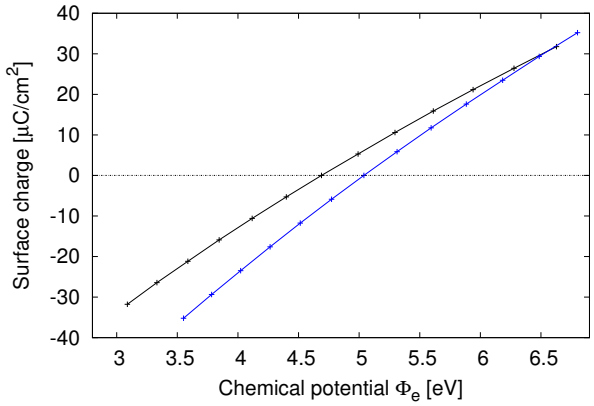

Figure S9: Surface charge versus the applied potential for Au(111) and Pt(111), shown in black and blue, respectively

change in the double layer capacity and reported values, generally correspond to mean values.

References

(S1) Mortensen, J. J.; Hansen, L. B.; Jacobsen, K. W. *Phys. Rev. B* **2005**, *71*, 35109.

(S2) Enkovaara, J.; Rostgaard, C.; Mortensen, J. J.; Chen, J.; Dułak, M.; Ferrighi, L.; Gavnholt, J.; Glinsvad, C.; Haikola, V.; Hansen, H. A.; Kristoffersen, H. H.; Kuisma, M.; Larsen, A. H.; Lehtovaara, L.; Ljungberg, M.; Lopez-Acevedo, O.; Moses, P. G.; Ojanen, J.; Olsen, T.; Petzold, V.; Romero, N. A.; Stausholm-Møller, J.; Strange, M.; Tritsaris, G. A.; Vanin, M.; Walter, M.; Hammer, B.; Häkkinen, H.; Madsen, G. K. H.; Nieminen, R. M.; Nørskov, J. K.; Puska, M.; Rantala, T. T.; Schiøtz, J.; Thygesen, K. S.; Jacobsen, K. W. *Journal of Physics: Condensed Matter* **2010**, *22*, 253202.

(S3) Dutta, B. N.; Dayal, B. *physica status solidi (b)* **1963**, *3*, 473–477.

(S4) Gross, A.; Schnur, S. *Catalysis in Electrochemistry*; John Wiley & Sons, Inc., 2011; Chapter 5, pp 165–196.

(S5) Sakong, S.; Naderian, M.; Mathew, K.; Hennig, R. G.; Groß, A. *The Journal of Chemical Physics* **2015**, *142*, 234107.

(S6) Bondi, A. *The Journal of Physical Chemistry* **1964**, *68*, 441–451.

(S7) Larsen, A. H.; Vanin, M.; Mortensen, J. J.; Thygesen, K. S.; Jacobsen, K. W. *Phys. Rev. B* **2009**, *80*, 195112.

(S8) Held, A.; Walter, M. *The Journal of Chemical Physics* **2014**, *141*, 174108.

(S9) Letchworth-Weaver, K.; Arias, T. A. *Phys. Rev. B* **2012**, *86*, 75140.